

Effects of incoming surface wind conditions on the wake characteristics and dynamic wind loads acting on a wind turbine model

Cite as: Phys. Fluids **26**, 125108 (2014); <https://doi.org/10.1063/1.4904375>

Submitted: 18 May 2014 • Accepted: 02 December 2014 • Published Online: 22 December 2014

 Wei Tian, Ahmet Ozbay and Hui Hu



View Online



Export Citation



CrossMark

ARTICLES YOU MAY BE INTERESTED IN

[Wind tunnel study of the wind turbine interaction with a boundary-layer flow: Upwind region, turbine performance, and wake region](#)

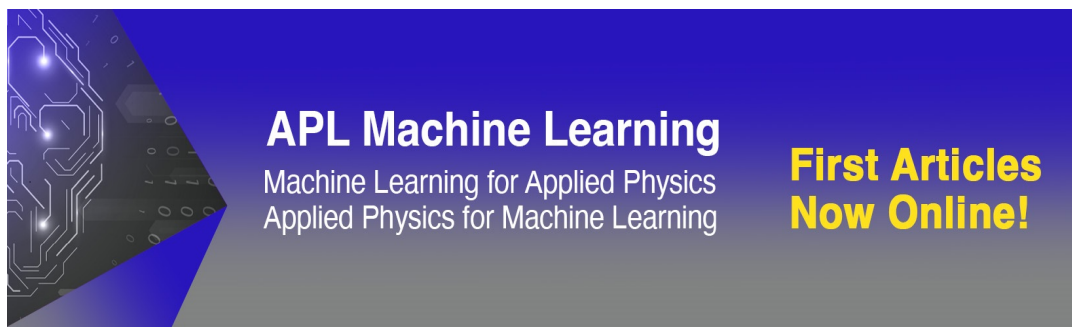
Physics of Fluids **29**, 065105 (2017); <https://doi.org/10.1063/1.4984078>

[Influence of atmospheric stability on wind-turbine wakes: A large-eddy simulation study](#)

Physics of Fluids **27**, 035104 (2015); <https://doi.org/10.1063/1.4913695>

[Experimental study of the horizontally averaged flow structure in a model wind-turbine array boundary layer](#)

Journal of Renewable and Sustainable Energy **2**, 013106 (2010); <https://doi.org/10.1063/1.3289735>



APL Machine Learning
Machine Learning for Applied Physics
Applied Physics for Machine Learning

**First Articles
Now Online!**

Effects of incoming surface wind conditions on the wake characteristics and dynamic wind loads acting on a wind turbine model

Wei Tian,^{1,2} Ahmet Ozbay,¹ and Hui Hu^{1,a)}

¹*Department of Aerospace Engineering, Iowa State University, Ames, Iowa 50010, USA*

²*School of Aeronautics and Astronautics, Shanghai Jiao Tong University, Shanghai 200240, China*

(Received 18 May 2014; accepted 2 December 2014; published online 22 December 2014)

An experimental investigation was conducted to examine the effects of incoming surface wind conditions on the wake characteristics and dynamic wind loads acting on a wind turbine model. The experimental study was performed in a large-scale wind tunnel with a scaled three-blade Horizontal Axial Wind Turbine model placed in two different types of Atmospheric Boundary Layer (ABL) winds with distinct mean and turbulence characteristics. In addition to measuring dynamic wind loads acting on the model turbine by using a force-moment sensor, a high-resolution Particle Image Velocimetry system was used to achieve detailed flow field measurements to characterize the turbulent wake flows behind the model turbine. The measurement results reveal clearly that the discrepancies in the incoming surface winds would affect the wake characteristics and dynamic wind loads acting on the model turbine dramatically. The dynamic wind loads acting on the model turbine were found to fluctuate much more significantly, thereby, much larger fatigue loads, for the case with the wind turbine model sited in the incoming ABL wind with higher turbulence intensity levels. The turbulent kinetic energy and Reynolds stress levels in the wake behind the model turbine were also found to be significantly higher for the high turbulence inflow case, in comparison to those of the low turbulence inflow case. The flow characteristics in the turbine wake were found to be dominated by the formation, shedding, and breakdown of various unsteady wake vortices. In comparison with the case with relatively low turbulence intensities in the incoming ABL wind, much more turbulent and randomly shedding, faster dissipation, and earlier breakdown of the wake vortices were observed for the high turbulence inflow case, which would promote the vertical transport of kinetic energy by entraining more high-speed airflow from above to re-charge the wake flow and result in a much faster recovery of the velocity deficits in the turbine wake. © 2014 AIP Publishing LLC. [<http://dx.doi.org/10.1063/1.4904375>]

I. INTRODUCTION

Wind energy, as a renewable energy source, has been playing an increasingly important role in worldwide energy production portfolio in recent years. Nowadays, with rapid development of wind energy, wind turbines sited in wind farms would operate under many different terrain conditions, ranging from rather flat sites such as open ocean terrain for offshore wind farms to complex hilly terrains for onshore wind farms.

There are vast discrepancies in the flow characteristics for the incoming atmospheric boundary layer (ABL) winds over typical onshore and offshore wind farms. While the near neutral ABL

^{a)}Email: huhui@iastate.edu

winds over offshore wind farms on relatively flat ocean surfaces are found to have relatively low ambient turbulence, the ABL winds over onshore wind farms have much higher ambient turbulence levels due to the effects of complex terrain topography, various roughness on the ground (e.g., buildings, trees, and plants), and the significant variations between highly convective daytime conditions and highly stable nocturnal conditions. As a result, the wind turbines sited in onshore wind farms would see quite different surface wind characteristics (i.e., different mean wind speed profiles with much higher turbulence levels) in comparison with those in offshore wind farms.

A number of studies have been conducted in recent years to reveal the effects of the turbulence intensity levels of the incoming surface winds on the aeromechanics performances of wind turbines as well as the characteristics of the wake flows behind the wind turbines. For example, Sheinman and Rosen¹ reported that the over-estimation of turbine power output could be more than 10% if ignoring the effects of turbulence in the incoming flow. Lebron *et al.*² studied the fluxes of kinetic energy on a wind turbine streamtube including the effects of turbulence. Their analysis results confirm that turbulence plays a central role in the energetics of a wind turbine streamtube. Chamorro and Porte-Agel³ showed that the effects of boundary layer turbulence on the velocity deficit and added turbulence intensity in the far wake behind a wind turbine model are not negligible even at a downwind distance of 15 times the rotor diameter. More recently, Ozbay *et al.*⁴ studied the effects of the turbulence intensity levels of the incoming airflows on the wake interferences among multiple wind turbines with different wind farm layouts. They reported that, with the same staggered wind farm configuration, the incoming surface flow with higher turbulence levels, corresponding to onshore wind farm case, would enhance the total power output of the wind farm by 6%, in comparison with the offshore wind farm case.

As described in the review article of Vermeer *et al.*,⁵ the wake behind a wind turbine is typically divided into a near wake and a far wake. In the near wake, the presence of the rotor is apparent by the number of blades, blade aerodynamics such as attached or stalled flows, 3-D effects, and tip vortices. Whale *et al.*,⁶ Grant and Parkin,⁷ and Massouh and Dobrev⁸ conducted experimental studies to investigate the flow structures in the near wakes of model turbines in airflows or water flows with uniform incoming flow velocity. Chamorro *et al.*⁹ and Yang *et al.*¹⁰ studied the evolution of the unsteady vortex and turbulent flow structures in the near wakes of wind turbines placed in nonhomogeneous ABL flows with rather high turbulence intensity levels. The findings reported in those previous studies reveal clearly that the turbine wake characteristics with the wind turbines placed in uniform incoming flows were found to be substantially different from those turbines sited in nonhomogeneous ABL flows with strong vertical velocity gradients and high turbulence intensity levels in the incoming flows.

As described in Massouh and Dobrev,⁸ the shedding of unsteady wake vortices in the near turbine wakes has been suggested as one of the important sources to induce turbine blade vibration, which is highly associated with the dynamic wind loads acting on the wind turbines. So far, the characteristics of dynamic wind loads acting on wind turbines are mainly obtained from field measurements of large-scale wind turbines. Based on analyzing the blade surface pressure distributions and local incoming flow data, Schreck and Robinson¹¹ characterized two key dynamic stall processes for wind turbines: vortex initiation and vortex convection. In the study of Robinson *et al.*,¹² blade surface pressure data were analyzed to characterize the impacts of three-dimensionality, unsteadiness, and flow separation effects observed to occur on downstream wind turbines. In addition, a number of numerical approaches have been implemented in order to predict the dynamic responses of wind turbines. For example, Moriarty *et al.*¹³ generated multiple samples of wind loading data under various wind conditions by using a stochastic turbulence simulator coupled with an aeroelastic code. More recently, Lee *et al.*¹⁴ used a two-way coupled aeroelastic tool with large eddy simulation (LES) to investigate the atmospheric and wake turbulence impacts on wind turbines.

Wind tunnel facilities have been widely used to study aeromechanics of wind turbines due to their capabilities to produce well-controlled flow conditions. Chamorro and Porte-Agel^{3,15} performed wind tunnel studies to investigate the effects of boundary layer turbulence as well as thermal stability on the wake of a single wind turbine sited in a boundary layer flow. The turbulence properties inside and above the aligned and staggered wind farms consisted by model wind turbines

were also systemically investigated by Chamorro and Porte-Agel.^{9,16} Lebron *et al.*¹⁷ conducted an experimental study on the interaction between a wind turbine array and turbulent boundary layer with the main objective of collecting velocity data in sufficient detail to address questions such as the mechanisms for kinetic energy entrainment into the wind turbine array field. Cal *et al.*¹⁸ carried out an experimental study of the horizontally averaged flow structure in a boundary layer flow including a 3×3 array of model wind turbines in order to understand the vertical transport of momentum and kinetic energy across a boundary layer flow with wind turbines. The attentions of these studies focused on wake models, wake interference, and turbulence models for far wake flows. More recently, Hu *et al.*¹⁹ conducted a comprehensive experimental study to quantify the dynamic wind loads and wake characteristics of a wind turbine model in an ABL wind. Zhang *et al.*²⁰ reported the detailed turbulent structures in the near wake of a wind turbine, including the characterization of the wake rotation effects and coherent tip vortex shedding.

In the present study, an experimental study is conducted to investigate the effects of the incoming flow conditions on the turbine wake characteristics and dynamic wind loads acting on a same model wind turbine placed in two types of ABL winds with distinct mean and turbulence characteristics to simulate the scenario with a same wind turbine sited in a typical onshore wind farm in comparison with that in a typical offshore wind farm. In addition to measuring dynamic wind loads acting on the model turbine, a high-resolution Particle Image Velocity (PIV) system is used to conduct detailed flow field measurements to quantify the turbine wake characteristics as well as the dependence of wake vortices on the rotation of the rotor blades with the model turbine sited in different non-homogenous incoming surface winds. The detailed flow field measurements are correlated with the dynamic wind load data in order to gain further insight into the underlying physics for the optimal design of wind turbines operating in different ABL winds.

II. EXPERIMENTAL SETUP AND PROCEDURE

The experimental study was performed in the Aerodynamic/Atmospheric Boundary Layer (AABL) Wind Tunnel located at the Aerospace Engineering Department of Iowa State University. The AABL wind tunnel is a closed-circuit wind tunnel with a test section 20 m long, 2.4 m wide, and 2.3 m high. It has a capacity of generating a maximum wind speed of 45 m/s in the test section. Figure 1 shows a picture of the test section of the AABL tunnel with triangular spires and arrays of wooden blocks on the wind tunnel floor to simulate the surface flow conditions similar to those in ABL winds over typical onshore and offshore wind farms. Similar as those used by Irwin,²¹ Sill,²² and Jia *et al.*²³ in their wind tunnel experiments to generate environmental boundary layer winds, five isosceles triangle shaped spires, which are equally distributed at the inlet of the test section of the AABL tunnel, were used in the present study to generate a mean velocity shear profile of the



FIG. 1. AABL wind tunnel used for the present study.

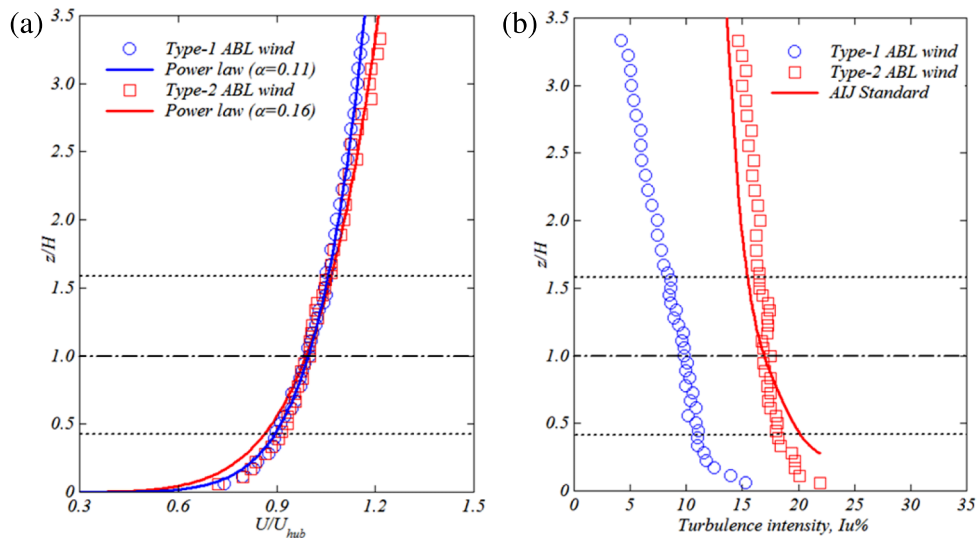


FIG. 2. Flow characteristics of the two different incoming ABL winds used in the present study: (a) mean streamwise velocity profiles and (b) turbulence intensity profiles.

incoming airflow in the test section. As shown in Fig. 1, a wooden plate with the height of 200 mm and thickness of 12.7 mm was mounted on the wind tunnel floor to connect to the five spires. In the present study, the spires with aspect ratios of 0.12 and 0.16 were used to generate two ABL winds with different velocity and turbulence intensity gradients. Surface roughness elements with different size and spacing were also mounted on the wind tunnel floor to generate different levels of turbulence intensity of the incoming ABL winds. By using different combinations of the roughness elements and triangle shaped spires, different ABL winds with distinct mean and turbulence characteristics can be generated in the AABL tunnel. The tunnel ceiling, which is flexible, was adjusted along the length to accommodate the boundary layer blockage to ensure a zero pressure gradient along the flow direction.

As described in Zhou and Kareem²⁴ and Jain,²⁵ the mean velocity profile of an ABL wind over an open terrain can usually be fitted well by using a power function. Different power-law exponents represent different types of winds over different terrains. Figure 2 gives the measured mean flow velocity and turbulence intensity profiles of the two different ABL winds generated in AABL wind tunnel for the present study. The measurement data were obtained by using a Cobra Probe Anemometry system (TFI Series 100 of Turbulent Flow Instrumentation Pty Ltd.) in the tunnel test section at the location where the model wind turbine would be mounted.

As shown in Fig. 2(a), the power-law exponent for the first type of ABL wind is about 0.11, which can be used to represent the ABL wind over offshore (open sea) terrain according to American Society of Civil Engineers (ASCE) standard.²⁶ The corresponding turbulence intensity shown in Fig. 2(b) at the turbine hub height ($Z/H = 1$) was found to be about 9.5% for the Type-1 ABL wind (i.e., low turbulence inflow case), which is in the range of the turbulence intensity levels measured over Horns Rev offshore wind farm as reported in Hansen *et al.*²⁷ Here, the turbulence intensity is calculated by using the expression of $I_u = \sigma_u/U_{local}$, where σ_u is the root-mean-square of the turbulent velocity fluctuations, and U_{local} is the mean wind speed at the measurement point. For the second type of the ABL wind, the power-law exponent of the mean velocity profile was found to be about 0.16, which can be used to represent the ABL wind over the terrain of open country with low scrub or scattered trees^{24,25} (e.g., the onshore wind farms in Midwest region of the USA). The turbulence intensity levels for the Type-2 ABL wind as a function of the height above the tunnel floor is also given in Fig. 2(b). The standard turbulence intensity profile of the ABL wind over an open terrain on land suggested by Architectural Institute of Japan (AIJ)²⁸ was also plotted in the graph for comparison. It can be seen clearly that, the turbulence intensity levels of the Type-2 ABL wind (i.e., high turbulence inflow case) used in the present study is in a fairly good agreement

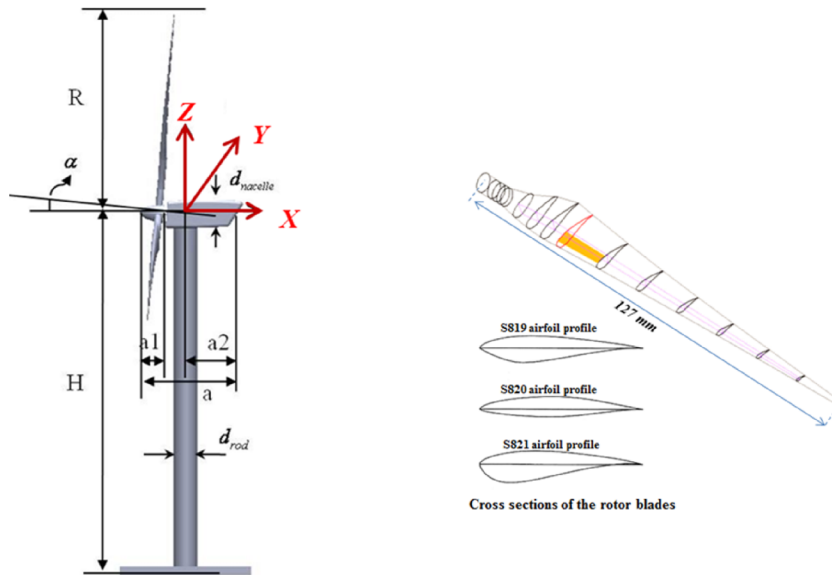


FIG. 3. The schematic of the wind turbine model used in the present study.

with the AIJ standard values for ABL over open terrain on land. It should also be noted that the turbulence intensity level at the turbine hub height for the Type-2 ABL wind is about 18.0%, which is almost twice as high as that of the Type-1 ABL wind.

The model wind turbine of the present study represents the most commonly used three-blade horizontal axial wind turbines (HAWTs) seen in modern wind farms. Figure 3 shows a schematic of the model wind turbine along with typical cross section profiles of the turbine rotor blades. The model turbine has a rotor radius of 140 mm and hub height of 225 mm. With the scale ratio of 1:320, the model turbine would represent 2 MW wind turbines commonly seen in modern wind farms with a rotor diameter of about 90 m and a tower height of about 80 m. The rotor blades of the model turbine are made of a hard plastic material by using a rapid prototyping machine. The rotor blades have the same airfoil cross sections and platform profiles as ERS-100 prototype turbine blades developed by TPI Composites, Inc. As shown in Fig. 3, the rotor blade has a constant circular cross section from the blade root to 5% blade radius (R), and three NREL airfoil profiles (S819, S820, S821) are used at different spanwise locations along the rotor blade. The S821 airfoil profile is used between $0.208R$ and $0.40R$, the S819 primary airfoil is positioned at $0.70R$, and the S820 airfoil profile is specified at $0.95R$. A spline function is used to interpolate the prescribed cross section profiles to generate the three dimensional model of the rotor blade using SolidWorks software. In the present study, the rotor blades were mounted on a turbine hub with a pitch angle of 3.0° . A DC electricity generator (Kysan, FF-050S-07330) was installed inside the nacelle of the model turbine, which would produce electricity as driven by the rotating blades. While primary design parameters of the model turbine are listed in Table I, further information about the ERS-100 rotor blades is available at Locke and Valencia.²⁹ It should be noted that, the blockage ratio of the model turbine (i.e., the ratio of the turbine blade swept area to the cross-section area of AABL tunnel) was found to be about 1.2%, and thus, the blockage effects of the model turbine in the test section of AABL is almost negligible for the present study.

TABLE I. The design parameters of the wind turbine model.

Parameter	R	H_{hub}	d_{rod}	$d_{nacelle}$	α	a	a_1	a_2
Dimension (mm)	140	226	18	26	5°	68	20	35

During the experiments, the mean wind speed at the hub height of the model turbine was set to be about 5.0 m/s (i.e., $U_{hub} = 5.0$ m/s). The Reynolds number based on the averaged chord length of the rotor blades (C) and the incoming wind speed at the hub height (U_{hub}) was found to be about 7000 (i.e., $Re_C \approx 7000$). It should be noted that this Reynolds number is significantly lower than those of large-scale wind turbines in the field, i.e., $Re_C \approx 7.0 \times 10^3$ for the present study vs. $Re_C > 1.0 \times 10^6$ for the large-scale wind turbines as described in Wilson.³⁰ According to Alfredsson *et al.*³¹ and Medici and Alfredsson,³² while the chord Reynolds number of a wind turbine may have a significant effect on the power production performance of the wind turbine (i.e., the maximum power coefficient would be much lower for a small-scale model turbine operating at a lower Reynolds number), the wake characteristics and the evolution of the unsteady vortices in the turbine wake would become almost independent of the chord Reynolds number when the chord Reynolds number of the model turbine is higher enough. De Vries³³ suggested a required minimum chord Reynolds number on the order of $Re_C = 3 \times 10^5$ for a reliable comparison of the model test results with full-scale data. More recently, Chamorro *et al.*³⁴ conducted a comprehensive study to quantify the Reynolds number dependence of turbulence statistics in the wake flow behind a model turbine sited in ABL winds. Instead of using chord Reynolds number, the Reynolds number based on the turbine rotor diameter (D) and the flow velocity at the turbine hub height (U_{hub}), i.e., Re_D , was used by Chamorro *et al.*³⁴ to characterize the wake measurement results. They found that fundamental flow statistics (i.e., normalized profiles of mean velocity, turbulence intensity, kinematic shear stress, and velocity skewness) in the turbine wake have asymptotic behavior with the Reynolds number. Mean velocity in the turbine wake was found to reach Reynolds number independence at a lower value compared to that of higher-order statistics (i.e., turbulence intensity, turbulent kinematic energy, and Reynolds shear stress). Reynolds number independence for mean velocity could be reached at $Re_D \approx 4.8 \times 10^4$, and that of higher order statistics started at $Re_D \approx 9.3 \times 10^4$. It should be noted that, the Reynolds number based on the rotor diameter of the turbine and the wind speed at the turbine hub height for the present study is about 90 000 (i.e., $Re_D \approx 9.0 \times 10^4$), which is in the range of the required minimum Reynolds number as suggested by Chamorro *et al.*³⁴ to achieve Reynolds number independence of the turbine wake statistics.

In the present study, the rotation speed of the turbine rotor blades was adjusted by applying different electric loads to the small DC generator installed inside the turbine nacelle. The turbine rotation speed Ω can change from 0 to 2200 rpm, and the tip-speed-ratio ($\lambda = \Omega R / U_{hub}$, where R is the radius of the rotor) of the model turbine is in the range from 0 to 6.5. During the experiments, a series of tip-speed-ratio values were adjusted to test the dynamic wind loads acting on model turbine. For the measurement results given in the present study, the model turbine was set to operate at the optimum tip-speed-ratio of $\lambda \approx 5.0$, i.e., at the tip-speed-ratio with the maximum power output of the model turbine. It should be noted that a typical three-blades HAWT on a modern wind farm usually has a tip-speed-ratio of $\lambda \approx 4.0 \sim 8.0$, as described in Burton *et al.*³⁵

For the model turbine used in the present study, an aluminum rod was used as the turbine tower to support the turbine nacelle and the turbine rotor blades. Through a hole on the wind tunnel floor, the aluminum rod was connected to a high-sensitivity force-moment sensor (JR3 load cell, model 30E12A-I40) to measure the dynamic wind loads (aerodynamic forces and bending moments) acting on the model turbine. The JR3 load cell is composed of foil strain gage bridges, which are capable of measuring the forces on three orthogonal axes, and the moment (torque) about each axis. The precision of the force-moment sensor cell for force measurements is $\pm 0.25\%$ of the full range (40 N). During the experiments, the wind load data were acquired for 120 s at a sampling rate of 1000 Hz for each test case. A Monarch Instrument Tachometer was also used to measure the rotation speed of the wind turbine blades independently.

In addition to the wind loading measurements, a high-resolution PIV system was also used in the present study to conduct detailed flow field measurements in the vertical plane passing through the symmetrical plane of the model turbine. Figure 4 gives the schematic of the experimental setup used for PIV measurements. For the PIV measurements, the incoming airflow was seeded with $\sim 1 \mu\text{m}$ oil droplets by using a droplet generator. Illumination was provided by a double-pulsed laser adjusted on the second harmonic and emitting two pulses of 200 mJ at the wavelength of 532 nm. The thickness of the laser sheet in the measurement region was about 1.0 mm. In order to have a

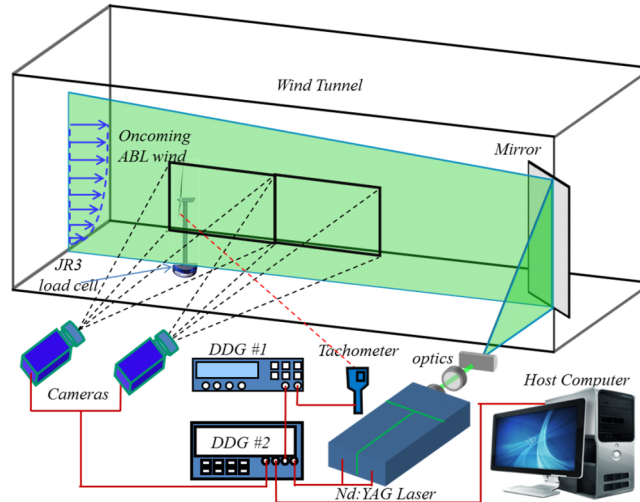


FIG. 4. Experimental setup used for PIV measurements.

larger measurement window along the streamwise direction to reveal the turbulent flow structures behind the model turbine, two high-resolution 16-bit CCD cameras (PCO1600, CookeCorp) were used for PIV image acquisition with the axis of the cameras perpendicular to the laser sheet. The CCD cameras and the double-pulsed Nd:YAG lasers were connected to a workstation (host computer) via a digital delay generator (Berkeley Nucleonics, Model 565), which controlled the timing of the laser illumination and the image acquisition.

After PIV image acquisition, instantaneous PIV velocity vectors were obtained by a frame to frame cross-correlation technique involving successive frames of patterns of particle images in an interrogation window of 32×32 pixels, which has a physical area of $7.4 \text{ mm} \times 7.4 \text{ mm}$. An effective overlap of 50% of the interrogation windows was employed in PIV image processing, which result in a spatial resolution of $3.7 \text{ mm} \times 3.7 \text{ mm}$ for the PIV measurements. After the instantaneous velocity vectors (u_i, v_i) were determined, the vorticity (ω_z) can be derived. The distributions of the ensemble-averaged flow quantities such as the mean velocity, normalized Reynolds Stress $(\bar{\tau} = -\overline{u'v'}/U_{hub}^2)$, and in-plane turbulence kinetic energy $(TKE = 0.5 * (\overline{u'^2} + \overline{v'^2})/U_{hub}^2)$ were obtained from the instantaneous PIV measurements. In the present study, a cinema sequence of 1000 frames of instantaneous PIV image pairs were obtained in order to ensure a good convergence of turbulence statistics of the PIV measurements such as TKE and Reynolds Stress. The measurement uncertainty level for the velocity vectors is estimated to be within 2%, while the uncertainties for the measurements of ensemble-averaged flow quantities such as Reynolds stress and turbulent kinetic energy distributions about 5%.

In the present study, both “free-run” and “phase-locked” PIV measurements were performed during the experiments. The “free-run” PIV measurements were conducted in order to determine the ensemble-averaged flow statistics (e.g., mean velocity, Reynolds Stress, and turbulence kinetic energy) in the turbine wake. For the “free-run” PIV measurements, the image acquisition rate was pre-selected at a frequency that is not a harmonic frequency of the rotating frequency of the turbine rotor blades in order to ensure physically meaningful measurements of the ensemble-averaged flow quantities. “Phase-locked” PIV measurements were conducted to elucidate more details about the dependence of unsteady wake vortices in relation to the position of the rotating rotor blades. For the “phase-locked” PIV measurements, a digital tachometer was used to detect the position of a pre-marked rotor blade. The tachometer would generate a pulsed signal as the pre-marked rotor blade passed through the vertical PIV measurement plane. The pulsed signal was then used as the input signal to a Digital Delay Generator (DDG) to trigger the digital PIV system to achieve the “phase-locked” PIV measurements. By adding different time delays between the input signal from the tachometer and the transistor-transistor logic (TTL) signal output from the DDG to trigger the

digital PIV system, the “phase-locked” PIV measurements at different rotation phase angles of the pre-marked rotor blade can be accomplished. At each pre-selected phase angle (i.e., corresponding to different positions of the pre-marked rotor blade related to the vertical PIV measurement plane), 200 frames of instantaneous PIV measurements were used to calculate the phase-averaged flow velocity distribution in the wake flow behind the model turbine. As shown in Fig. 4, since two CCD cameras were used for PIV image acquisition in order to have a larger measurement window along the streamwise direction, a standard linear regression method was used in the present study to determine the PIV measurement results in the overlap regions between the two PIV measurement windows. In the present study, a Cobra Probe Anemometry system (TFI Series 100 of Turbulent Flow Instrumentation Pty Ltd.), which is capable of measuring all three components of instantaneous flow velocity vector at a prescribed point with a sampling rate of up to 2.0 KHz, was also used to provide time-resolved flow velocity measurement data at the points of interest to supplement the PIV measurements.

III. EXPERIMENTAL RESULTS AND DISCUSSIONS

A. Dynamic wind load measurement results

As described above, the JR3 force-moment sensor used in the present study can provide time-resolved measurements of all three components of the aerodynamic forces and the moment

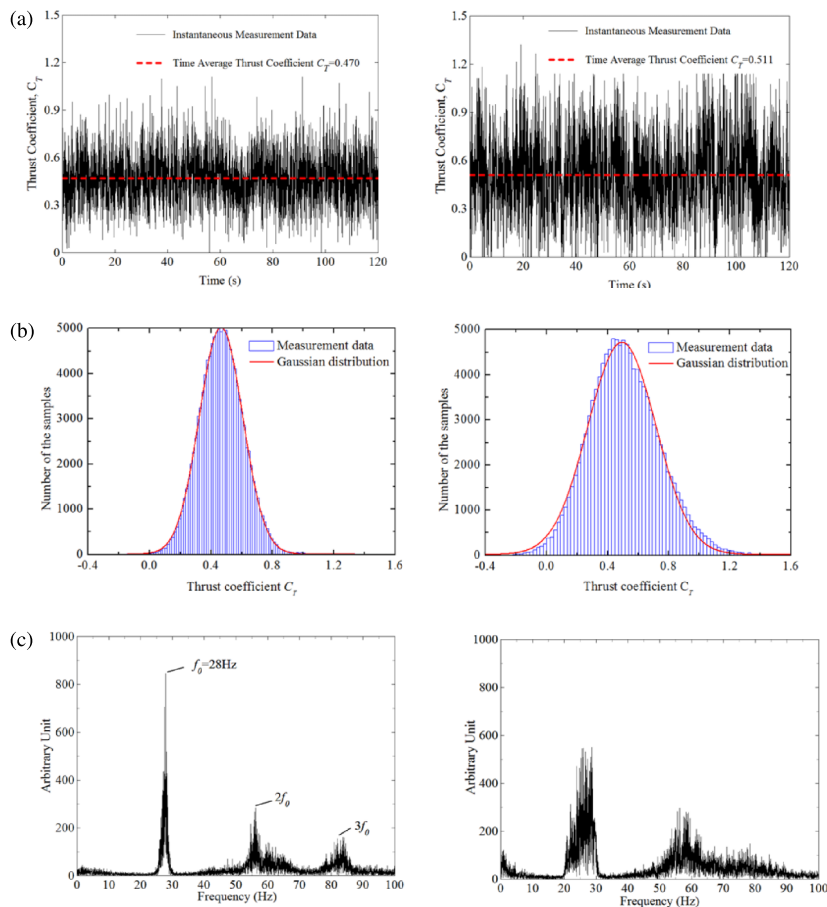


FIG. 5. Measurement results of the dynamic thrust force acting on the model wind turbine. Left: Low turbulence inflow case; Right: High turbulence inflow case. (a) Time history of the instantaneous thrust force, (b) histogram of the instantaneous thrust force, and (c) power spectrum of the dynamic thrust force.

(torque) about each axis. While similar features were also revealed by the other components of the aerodynamic forces and the moments, only the measured thrust coefficient, C_T , is given in the present study for analysis for conciseness. The thrust coefficient (i.e., aerodynamic force coefficient along X -direction for the Cartesian coordinate system given in Fig. 3) is defined as $C_T = T / (\frac{1}{2} \rho U_{hub}^2 \pi R^2)$, where ρ is the density of air, R is the radius of the wind turbine rotor, T is the thrust force acting on the model turbine. Figure 5 gives examples of the wind load measurement results in term of the instantaneous thrust coefficients with the model turbine sited in two different types of ABL winds. As revealed clearly from the time histories of the measured instantaneous thrust force given in Fig. 5(a), the wind loads acting on the model turbine in turbulent ABL winds (i.e., for both the Type-1 and Type-2 ABL winds) were found to be highly unsteady with their magnitudes fluctuating significantly as a function of time. The time-averaged values were also given in the plots as the dashed lines for comparison. It can be seen that the instantaneous wind loads acting on the turbine could be significantly higher compared with their mean values. Furthermore, while the mean value of the wind loads acting on the turbine sited in the incoming ABL wind with relatively low turbulence intensity levels (i.e., $C_T = 0.470$ for Type-1 ABL wind case) is only slight lower than that of the case with much higher turbulence intensity levels in the incoming ABL wind (i.e., $C_T = 0.511$ for Type-2 ABL wind case), the fluctuation amplitudes of the instantaneous wind loads acting on the turbine were found to become significantly higher for the high turbulence inflow case, in comparison with those of the relatively low turbulence inflow case.

Figure 5(b) shows the histograms of the measured instantaneous thrust forces acting on the model turbine, which can be used as an indicator to provide further insight about the effects of the incoming flow conditions on the dynamic wind loads acting the wind turbine. While the instantaneous wind loads acting on the model turbine were found to be highly unsteady with their magnitude fluctuating randomly as shown in Fig. 5(a), the histograms of the measured thrust force coefficients were found to be fitted reasonably well by using Gaussian functions for both the low and high turbulence inflow cases. It suggests that the standard deviation of the dynamic wind loads can be used as a quantitative parameter to evaluate the fatigue loads acting on wind turbines even though the turbines were sited in turbulent ABL winds. While the standard deviation value of the instantaneous thrust coefficient for the low turbulence inflow case was found to be about 0.14 (i.e., $\sigma = 0.14$), the corresponding value was found to become 0.23 (i.e., $\sigma = 0.23$) for the high turbulence inflow case, which is about 1.7 times of the low turbulence inflow case. The larger fluctuations of the dynamic wind loads would indicate much severe fatigue loads acting on the wind turbine when sited in onshore wind farms, which is believed to be closely related to the much higher turbulence intensity levels in the incoming ABL winds over the onshore wind farms. Such quantitative wind loading measurement results highlight the importance of taking the ambient turbulence intensity levels into account for the optimal mechanical design of the wind turbines operating in different ABL winds.

Figure 5(c) shows the power spectra of the measured instantaneous thrust forces acting on the model turbine through a fast Fourier transform (FFT) analysis procedure. For the case with relatively low turbulence intensity levels in the incoming flow, a well-defined dominant peak at $f_0 = 28$ Hz can be identified clearly in the spectrum plot, corresponding to the rotational speed of the turbine rotor blades at the optimum tip-speed-ratio of $\lambda \approx 5.0$. The rotational frequency of $f_0 = 28$ Hz based on the FFT analysis of the dynamic wind load measurements was found to agree very well with the independently measured rotational speed of the turbine blades by using a tachometer. Other peaks, representing the harmonic frequencies of the turbine blade rotational frequency f_0 , can also be identified clearly from the spectrum plot. However, for the case with much higher turbulence intensity levels in the incoming ABL wind, no well-defined dominant peaks can be identified in the corresponding power spectrum. Since the rotational speed of the turbine rotor blades was found to fluctuate greatly in a wide frequency region (i.e., $21 \text{ Hz} < f_0 < 30 \text{ Hz}$), a group of peaks can be seen in the power spectrum for the high turbulence inflow case. The significant fluctuations in the rotational speed of the turbine rotor blades would cause much more random shedding of the tip and root vortices from the turbine rotor blades, which were visualized clearly from the “phase-locked” PIV measurements to be discussed later. The significant fluctuations in the rotational speed of the turbine rotor blades would also result in much greater variations of the

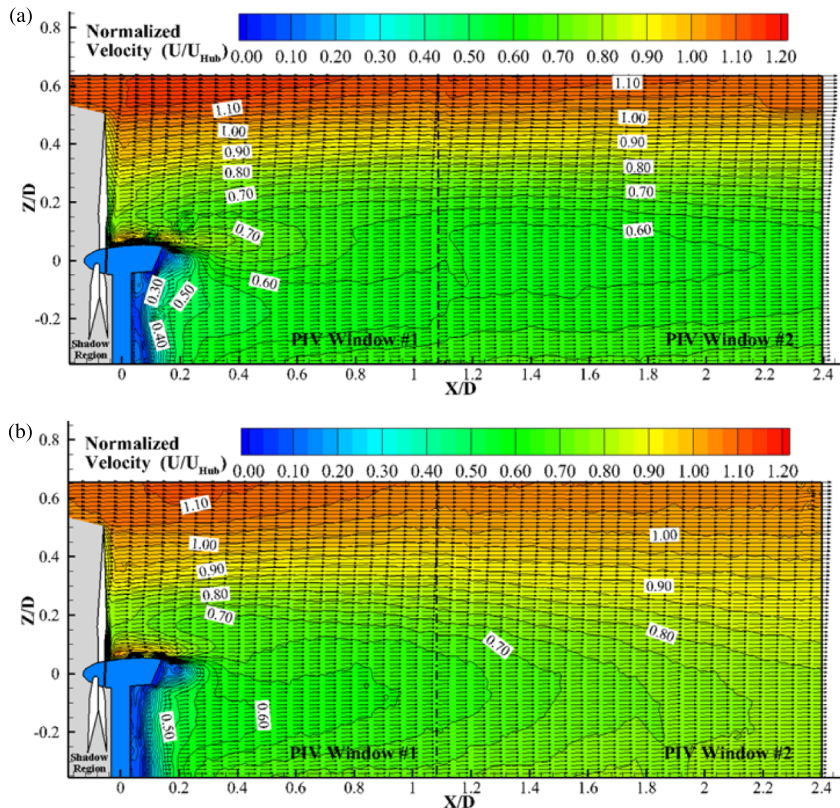


FIG. 6. Ensemble-averaged velocity distributions in the turbine wake: (a) for the low turbulence inflow case and (b) for the high turbulence inflow case.

dynamic wind loads, thereby, higher fatigue loads acting on the wind turbine for the high turbulence inflow case due to the almost doubled turbulence intensity levels in the incoming ABL wind.

B. “Free-run” PIV measurement results

As described above, “free-run” PIV measurements were conducted in the present study in order to determine the ensemble-averaged flow statistics (e.g., mean velocity, turbulence kinetic energy, and Reynolds Stress) in the turbine wake. Figure 6 shows the “free-run” PIV measurements in term of ensemble-averaged flow velocity distributions in the turbine wake for the low and high turbulence inflow cases. Figure 7 gives the transverse profiles of the mean flow velocity extracted from the PIV measurement results at the downstream locations of $X/D = 0.5, 1.0, 1.5,$ and 2.0 , respectively. The mean velocity profiles of the incoming ABL winds for the two tested cases were also plotted in the graphs for comparison. It can be seen clearly that, in comparison with the flow velocity profiles of the incoming ABL winds, obvious velocity deficits can be observed in the wake flow behind the wind turbine for both the low and high turbulence inflow cases. The size of the regions with significant velocity deficits were found to be much greater than that can be expected from the stationary turbine nacelle only. The incoming airflow streams were found to decelerate greatly as they pass through the rotation disk of the turbine blades since a portion of the kinetic energy carried by the incoming ABL winds was harvested by the wind turbine.

As shown clearly in Fig. 6(a), for the case with relatively low turbulence levels in the incoming ABL wind, the region with relatively low flow velocity (i.e., $U/U_{hub} < 0.7$) in the turbine wake were found to be elongated greatly, which extends beyond the PIV measurement window of the present study (i.e., $X/D > 2.4$). The iso-velocity contour lines for $U/U_{hub} > 0.7$ in the turbine wake were found to be almost parallel to each other in the downstream region of $1.0 < X/D < 2.0$.

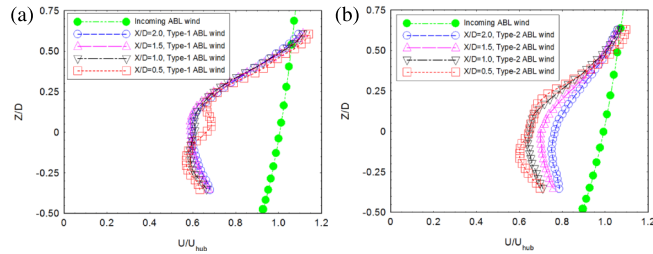


FIG. 7. Transverse velocity profiles in the turbine wake at different downstream locations: (a) for the low turbulence inflow case and (b) for the high turbulence inflow case.

As shown in Fig. 7(a), very little changes can be observed among the transverse mean velocity profiles extracted at different downstream locations. It indicates that the velocity deficits in the turbine wake would need a much longer distance to recover. However, as shown in Fig. 6(b), for the case with much higher turbulence levels in the incoming ABL wind, the size of the region with lower flow velocity (i.e., $U/U_{hub} < 0.7$) was found to become much smaller, in comparison with that of the low turbulence inflow case. The transverse mean velocity profiles extracted at different downstream locations were found to become quite different due to the much faster recovery of the velocity deficits in the turbine wake for the high turbulence inflow case.

Figure 8 shows the changes of the flow velocity of the turbine wake at the turbine hub height as a function of the downstream distance away from the rotation disk of the model turbine. The effects of the discrepancies in the incoming flow conditions on the recovery of the velocity deficits in the turbine wake can be seen more clearly from the comparison of the measurement results for the low and high turbulence inflow cases. As shown in Fig. 8, while passing through the recirculation zone at the downstream of the turbine nacelle, the wake flow velocity at the turbine hub height would increase very rapidly at the immediate downstream of the turbine nacelle (i.e., $X/D < 0.3$) for both the low and high turbulence inflow cases. The variations of the wake flow velocity at the turbine hub height were found to be quite different for the two compared cases at further downstream. For the low turbulence inflow case, the wake flow velocity at the turbine hub height was found to decrease slightly in the region of $0.4 < X/D < 1.5$ due to the expansion of the turbine wake and then increase slowly with the increasing downstream distance at further downstream (i.e., $X/D > 1.5$) due to the turbulent mixing in the turbine wake. For the high turbulence inflow case, while the wake flow velocity at the turbine hub height was found to have almost a constant value in the region of $0.4 < X/D < 1.0$, then increase monotonically with a much greater increase rate at further downstream (i.e., $X/D > 1.0$). As a result, the wake velocity at the turbine hub height for the high turbulence inflow case was found to become much greater than that of the low turbulence inflow case in the turbine wake further away from the wind turbine model (i.e., $X/D > 1.0$). The PIV measurement results given above reveal clearly that, at a same given downstream distance away from the upstream wind turbine, the velocity deficits in the turbine wake would recover much faster for the high turbulence inflow case than the low turbulence inflow case. It implies that, for the same given distance between the upstream and downstream wind turbines, the power losses for the downstream wind turbines due to the effects of the wake interferences of the upstream turbines would be much less with the turbines sited in ABL winds with much higher turbulence levels (e.g., onshore wind farm scenario), in comparison with the cases with lower turbulence levels in the ABL incoming winds (e.g., offshore wind farm scenario).

Figure 9 shows the normalized in-plane Turbulence Kinetic Energy ($TKE = 0.5 * (\overline{u'^2} + \overline{v'^2}) / U_{hub}^2$) distributions in the turbine wake for the low and high turbulence inflow cases, which can provide insights to explain the differences in the wake velocity deficit recovery for the two compared cases. It should be noted that, the color bar ranges given in Figs. 9(a) and 9(b) are different due to the significant differences of the TKE levels in the turbine wake for the compared cases. As shown in Fig. 9, while the distribution pattern of the TKE in the turbine wake was found to be quite similar for both the low and high turbulence inflow cases, the absolute TKE values in the turbine

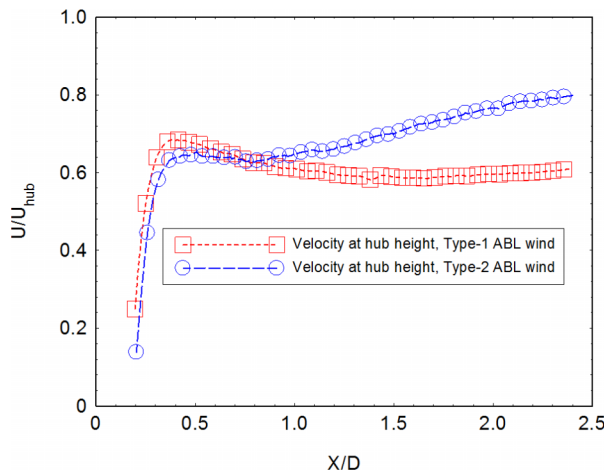


FIG. 8. The flow velocity at the turbine hub height as a function of the downstream distance.

wake for the high turbulence inflow case were found to be about 2–3 times greater than those of the low turbulence inflow case. The regions with quite high *TKE* levels were found to concentrate in the wake immediately behind the nacelle and tower of the wind turbine, which is believed to be closely related to the formation and shedding of unsteady wake vortices from the turbine nacelle and tower. The formation and shedding of unsteady wake vortices are visualized more clearly from the “phase-locked” PIV measurement results to be discussed later. *TKE* levels were also found to be quite high at the upper region behind the rotation disk of the turbine blades, which is correlated well to the shedding paths of the unsteady tip and root vortices from the rotating rotor blades in the PIV measurement plane. The expansion of the turbine wake with the increasing downstream distance away from the turbine rotor disk can also be observed in the measured *TKE* distributions.

As described above, the absolute levels of *TKE* in the turbine wake for the high turbulence inflow case were found to be much higher, in comparison with those of the low turbulence inflow case. *TKE* level can usually be used as a parameter to indicate the extent of turbulent mixing in a turbulent flow. The much higher *TKE* levels for the high turbulence inflow case would indicate much more intensive mixing in the turbine wake, corresponding to a much faster recovery of the velocity deficits in the turbine wakes for the high turbulence inflow case, in comparison with that of the low turbulence inflow case.

Since both the turbulence levels of the incoming ABL winds and the unsteady shedding of the complex wake vortices would contribute to the elevated turbulence levels in the turbine wake, the wake-vortex-induced *TKE* distributions in the turbine wake were determined in the present study in order to assess of the effects of the unsteady wake vortices on the characteristics of turbine wake flows more clearly. The wake-vortex-induced *TKE* values were obtained by subtracting the *TKE* levels of the incoming airflow from those of the measured *TKE* values in the turbine wake (i.e., $\Delta TKE = TKE_{wake\ flow} - TKE_{incoming\ ABL\ wind}$). Figure 10 gives the wake-vortex-induced *TKE* distributions for the low and high turbulence inflow cases. It can be seen that the behavior of wake-vortex-induced *TKE* in the near wake (i.e., the region of $X/D < 1.0$) and farther downstream (i.e., the region of $X/D > 1.0$) are quite different for the two compared cases. In the near wake region (i.e., $X/D < 1.0$), the wake-vortex-induced *TKE* levels in the region at the tip-top height of the turbine wake near to the turbine model ($X/D < 0.60$) were found to be slightly smaller for the high turbulence inflow case, in comparison with those of the low turbulence inflow case. For the high turbulence inflow case, the wake-vortex-induced *TKE* values were found to become negative in the region downstream of the roots of the rotor blades (i.e., $Z/D \approx 0.2$). It suggests that, due to the existence of the wind turbine, the *TKE* levels in the near region behind the wind turbine would become even smaller than those of the incoming ABL wind. A similar feature was also reported by Chamorro and Porte-Agel,³ who conducted wake flow measurements by using a pointwise cross-wire anemometer. In the region farther away from the wind turbine (i.e., $X/D > 1.0$), the

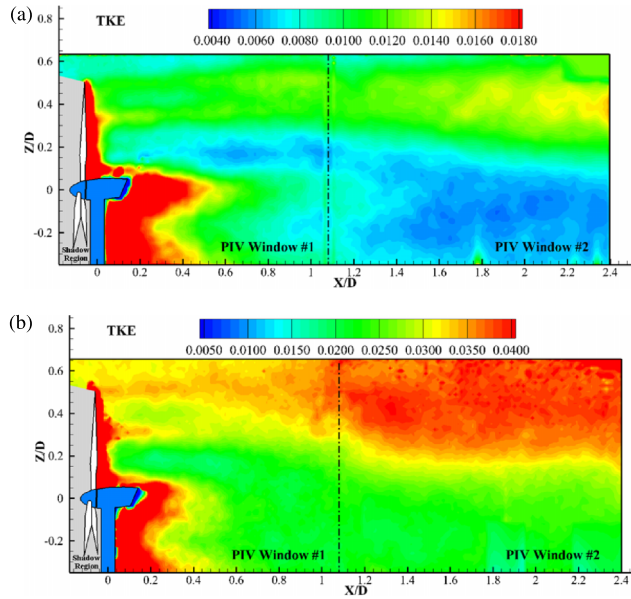


FIG. 9. Normalized TKE distributions in the turbine wake: (a) for the low turbulence inflow case and (b) for the high turbulence inflow case.

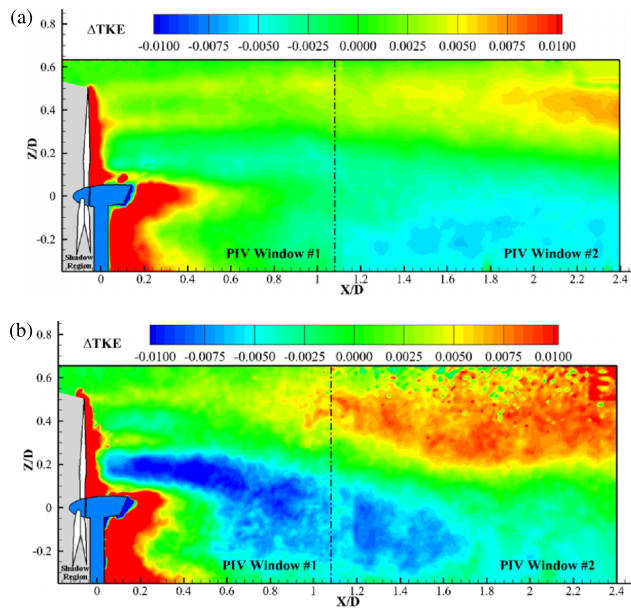


FIG. 10. Wake-vortex-induced turbulent kinetic energy (ΔTKE) distributions in the turbine wake: (a) for the low turbulence inflow case and (b) for the high turbulence inflow case.

wake-vortex-induced TKE values were found to become much higher for the high turbulence inflow case, which is adverse to the behavior of the wake-vortex-induced TKE in the near wake. Since the characteristics of the TKE distributions are closely related to the behavior of the unsteady vortex and turbulent structures in the turbine wake, further analysis about the characteristics of the TKE distributions in the turbine wake for the two compared cases will be given in the later section of “phase-locked” PIV measurement results.

Figure 11 gives the measured Reynolds stress distributions in the turbine wake for the low and high turbulence inflow cases. As suggested by Cal *et al.*,¹⁸ a higher Reynolds stress level would play an important role in promoting the vertical transport of the kinetic energy in a turbine wake,

which will draw down more high velocity airflow from above to the boundary layer flow. As shown in Fig. 11, while the distribution features of the Reynolds stress in the turbine wake for the low turbulence inflow case were found to be quite similar to those of the high turbulence inflow case, the absolute values of the Reynolds stress in the turbine wake for the high turbulence inflow case were found to be almost three times as high as those of the low turbulence inflow, i.e., the ranges of the color bars were different in plotting Figs. 11(a) and 11(b). In addition, the expansion of the regions with high Reynolds stress values at the upper portion of the turbine wake was also found to be much more aggressive for the high turbulence inflow case, in comparison with the low turbulence inflow case.

Based on the comparisons of the *TKE* and Reynolds stress distributions described above, it can be summarized that, due to the significant differences in the incoming flow conditions (i.e., distinct mean velocity and turbulence characteristics) for the two compared cases, the *TKE* and Reynolds stress levels in the turbine wake for the high turbulence inflow case would become much higher than those of the low turbulence inflow case, which would promote the vertical transport of kinetic energy by entraining more high-speed airflow from above to re-charge the wake flow behind the wind turbine. As a result, the velocity deficits in the turbine wake for the high turbulence inflow case would recover much faster than that of the low turbulence inflow case, as shown quantitatively in Fig. 6 to Fig. 8.

C. “Phase-locked” PIV measurement results

In the present study, “phase-locked” PIV measurements were also conducted to produce “frozen” images of the unsteady vortex structures in the turbine wake at different phase angles, from which the dependence of unsteady wake vortices on the rotation of the blades can be revealed more clearly and quantitatively. Figures 12 and 13 show the phase-averaged velocity distributions in the turbine wake at four different phase angles with the model turbine operating in the two different incoming surface winds. In the present study, the phase angle is defined as the angle between the vertical PIV measurement plane and the position of a pre-marked turbine rotor blade. The pre-marked rotor blade would be in the most upward position (i.e., within the vertical PIV measurement plane) at the phase angle of $\theta = 0^\circ$. As the phase angle increases, the turbine blade would rotate out of the vertical PIV measurement plane. As shown clearly in Fig. 12, the existence

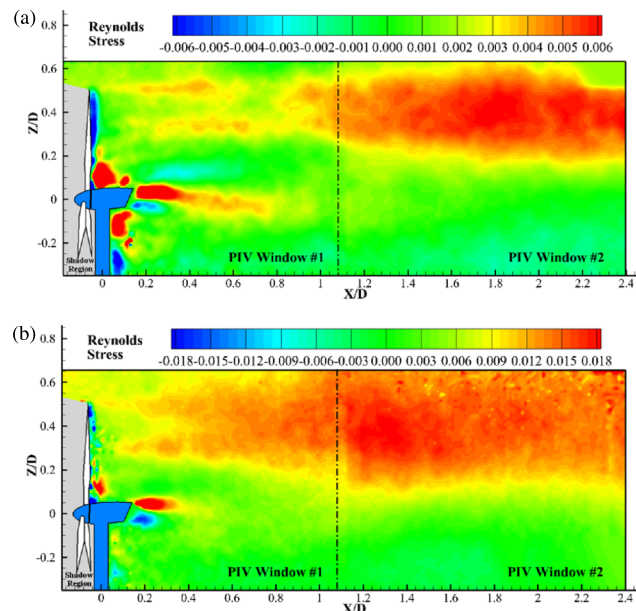


FIG. 11. Reynolds stress distributions in the turbine wake: (a) for the low turbulence inflow case and (b) for the high turbulence inflow case.

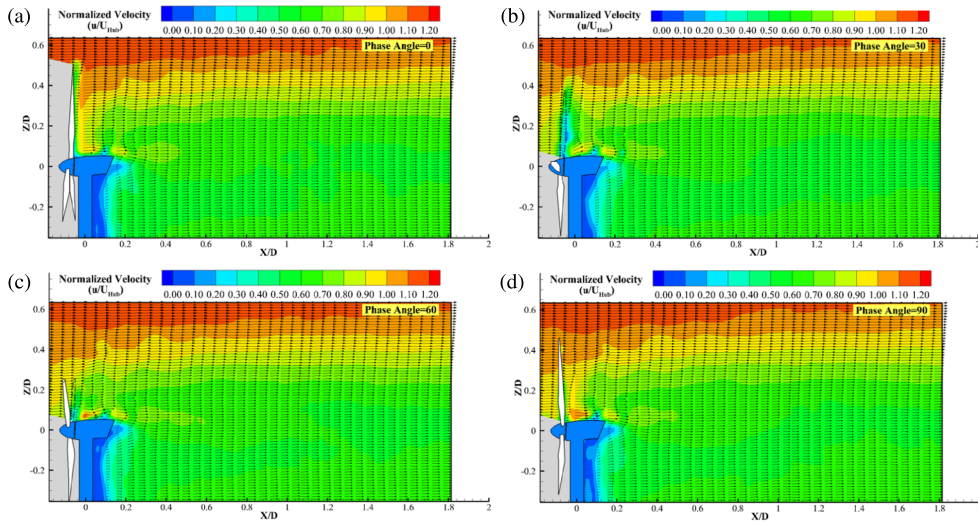


FIG. 12. “Phase-locked” flow velocity distributions for the low turbulence inflow case: (a) $\theta = 0^\circ$, (b) $\theta = 30^\circ$, (c) $\theta = 60^\circ$, and (d) $\theta = 90^\circ$.

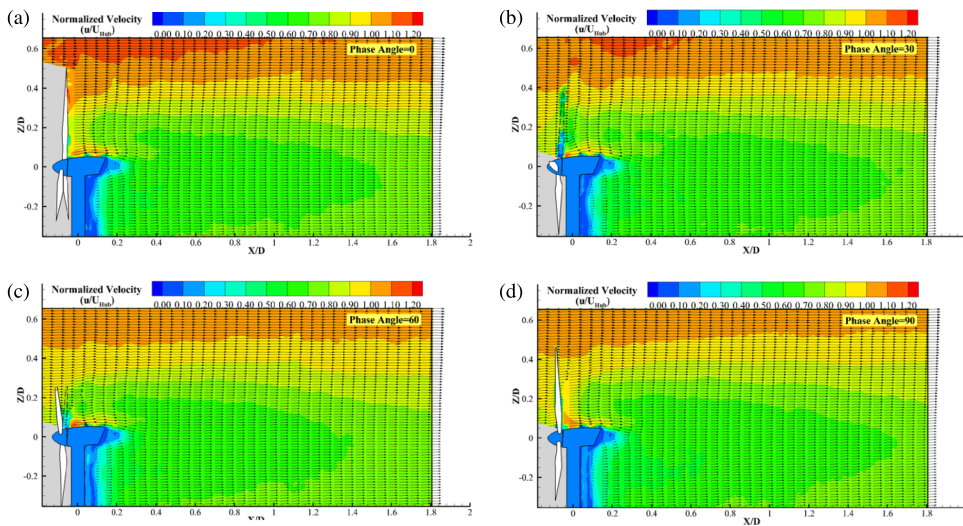


FIG. 13. Phase-locked flow velocity distributions for the high turbulence inflow case: (a) $\theta = 0^\circ$, (b) $\theta = 30^\circ$, (c) $\theta = 60^\circ$, and (d) $\theta = 90^\circ$.

of “wave-shaped” flow structures can be observed at the tip-top height in the turbine wake for the low turbulence inflow case, which is closely related to the formation and periodical shedding of tip vortices in the turbine wakes as suggested in Hu *et al.*¹⁹ The “wave-shaped” flow structures were found to propagate downstream as the phase angle increases. However, as shown in Fig. 13, the periodicity of the “wave-shaped” flow structures at the tip-top height in the turbine wake was found to become much less pronounced for the high turbulence inflow case. The “wave-shaped” flow structures were found to be dissipated rapidly as they move downstream, and become almost indistinguishable in the downstream region of $X/D > 0.5$ for the high turbulence inflow case.

Figures 14 and 15 show the “phase-locked” vorticity distributions in the turbine wake, which were derived from the “phase-locked” velocity distributions at different phase angles, for the low and high turbulence inflow cases, respectively. The effects of the discrepancies in the incoming surface wind conditions on the evolution of the unsteady wake vortex and turbulent flow structures in the turbine wake can be seen more clearly from the comparisons of the “phase-locked” vorticity

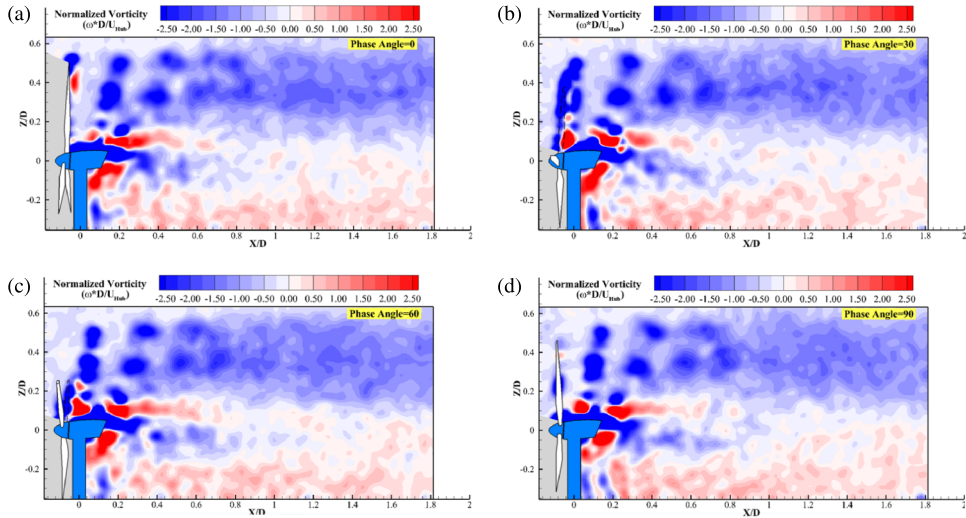


FIG. 14. Phase-locked vorticity distributions in the wake for the low turbulence inflow case: (a) $\theta = 0^\circ$, (b) $\theta = 30^\circ$, (c) $\theta = 60^\circ$, and (d) $\theta = 90^\circ$.

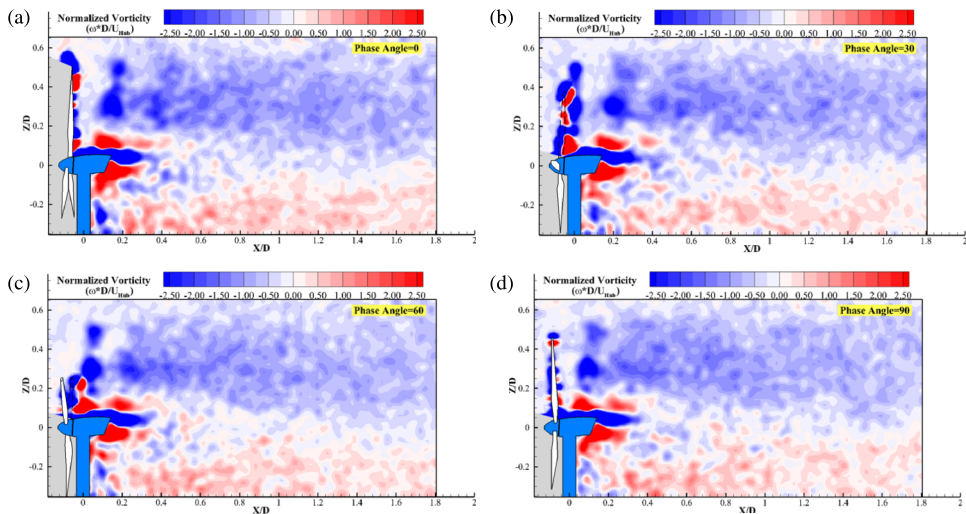


FIG. 15. Phase-locked vorticity distributions in the wake for the high turbulence inflow case: (a) $\theta = 0^\circ$, (b) $\theta = 30^\circ$, (c) $\theta = 60^\circ$, and (d) $\theta = 90^\circ$.

distributions. As shown in the figures, the wake flow behind the wind turbine is actually a very complex vortex flow, which is fully filled with various wake vortex structures with different spatial and temporal scales. In addition to the tip vortices and root vortices shedding periodically at the tips and roots of the turbine blades, unsteady vortex structures were also found to be generated on the upper and lower surfaces of the turbine nacelle as well as the von-Karman vortex streets shedding from the turbine tower. The flow characteristics in the wake behind the wind turbine were found to be dominated by the evolution (i.e., formation, shedding, and breakdown) of the unsteady wake vortices.

As described above, the pre-marked turbine blade would be within the vertical PIV measurement plane at the phase angle of $\theta = 0^\circ$. As shown clearly in Figs. 14 and 15, a tip vortex would be induced at the tip of the pre-marked turbine blade at the phase angle of $\theta = 0^\circ$. As the phase angle increases, while the pre-marked turbine blade rotates out of the vertical PIV measurement plane, the tip vortex was found to shed from the tip of the turbine rotor blade. While moving downstream,

the tip vortex was found to align itself nicely with other tip vortices induced by the other two rotor blades to form a moving tip vortex array in the wake flow. Besides the vortex array aligned nicely at the top-tip height of the rotor blades, an additional row of concentrated vortex structures were also found to be generated at the inboard of the turbine blades at approximately 50%–60% span of the rotor blades. The vortex structures were found to move outward with the expansion of the wake flow as they move downstream, and finally merge with the tip vortex structures. Similar vortex structures at approximately 50%–60% span of the rotor blades were also observed by Whale *et al.*⁶ and Hu *et al.*¹⁹ in their experimental studies to examine the evolution of unsteady wake vortex structures in turbine wake flows.

The influences of the different characteristics of the incoming ABL winds on the unsteady vortex structures in the turbine wake were revealed very clearly through the comparison of the “phase-locked” vorticity distributions for the low turbulence inflow case with those of the high turbulence inflow case. As shown in Fig. 14, for the low turbulence inflow case, concentrated vortices (i.e., both the tip vortices and the vortex structures at 50%–60% span of the rotor blades) shedding from the turbine rotor blades would align themselves nicely to form moving vortex arrays in the turbine wake, which were observed as the “wave-shaped” flow structures in the “phase-locked” flow velocity distributions given in Fig. 12. For the low turbulence inflow case, the wake vortex structures were found to be dissipated gradually as they move downstream, and eventually breakdown at the downstream location around $X/D \approx 0.8$.

For the high turbulence inflow case, as shown in Fig. 15, the concentrated wake vortices shedding from the turbine rotor blades (i.e., both the tip vortices and the vortex structures at 50%–60% span of the rotor blades) seem to become slightly weaker and smaller, in comparison with those of the low turbulence inflow case. The shedding of the wake vortices was also found to become much more turbulent and random for the high turbulence inflow case, due to the much higher turbulence intensity levels in the incoming airflow. All the observations are believed to be closely related to the much greater variations in the turbine rotational speed for the high turbulence inflow case, as revealed from the power spectrum analysis of the dynamic wind loads given in Fig. 5. For the high turbulence inflow case, the wake vortices, as travelling downstream, were found to be dissipated much more rapidly, and break down much earlier. As a result, the “wave-shaped” structures in the turbine wake for the high turbulence inflow case were found to become almost indistinguishable at the downstream location of $X/D \geq 0.4$ in the phase-locked flow velocity distributions, as shown in Fig. 13.

As described above, since the wake-vortex-induced *TKE* in the turbine wake would be determined by the behavior of the wake vortices, the wake-vortex-induced *TKE* and Reynolds stress levels in the turbine wake were found to be much higher in the regions along the shedding paths of the wake vortices structures. Corresponding to the weaker wake vortices in the turbine wake for the high turbulence inflow case as shown in Fig. 15, the wake-vortex-induced *TKE* levels in the near wake would be slightly lower than those of the low turbulence inflow case, as shown clearly in Fig. 10. Medici³⁶ conducted an experimental study to investigate the self-induced mixing properties in a turbine wake, and suggested that the existence of concentrated tip vortices in a turbine wake would prevent the wake flow from mixing with the outer high-speed airflow. As shown in Figs. 14 and 15, the concentrated wake vortices would break down at the downstream location of $X/D \approx 0.8$ for the low turbulence inflow case and at the downstream location of $X/D \approx 0.4$ for the high turbulence inflow case. After the breakdown of the concentrated wake vortices, the *TKE* and Reynolds stress levels in the turbine wake were found to increase dramatically. Since the higher *TKE* and Reynolds stress levels in the turbine wake would suggest more turbulent and intensive mixing in the turbine wake, it will be promoting the vertical transport of kinetic energy to entrain high-speed airflow from above to re-charge the wake flow. Corresponding to the much earlier breakdown of the concentrated wake vortices and much higher *TKE* and Reynolds numbers levels in the turbine wake, the recovery of the velocity deficits in the turbine wake for the high turbulence inflow case were found to be much faster, in comparison with that of the low turbulence inflow case, as shown clearly and quantitatively in Fig. 6 to Fig. 8.

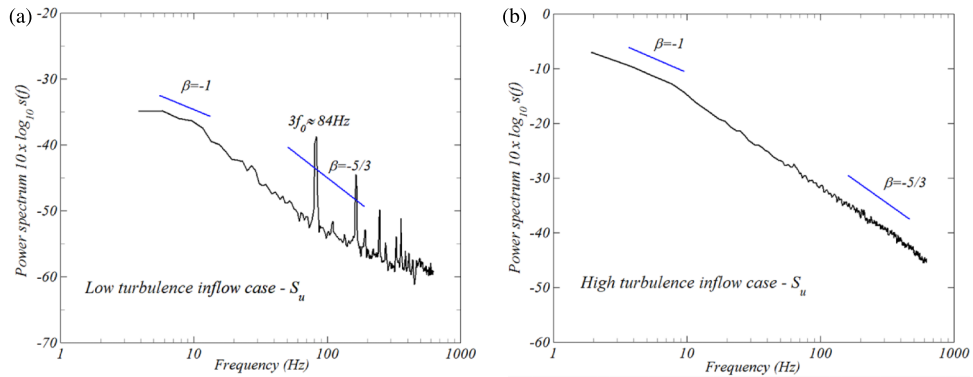


FIG. 16. Power spectra of the turbulent flow velocity in the turbine wake measured at the downstream location of ($X/D = 0.5$, $Y/D = 0.0$, and $Z/D = 0.5$): (a) for the low turbulence inflow case and (b) for the high turbulence inflow case.

D. Power spectra of the turbulent flow velocity in the turbine wake

As described above, a Cobra Probe Anemometry system was also used in the present study to provide time-resolved flow velocity measurement data at the points of interest to supplement the PIV measurements. By taking the FFT of the instantaneous flow velocity (u , v , and w) measured by using the Cobra Probe Anemometry system, a comparative study based on spectral analysis of the turbulent flow velocity in the turbine wake was also performed to assess the characteristics of the turbulence energy distributions across a range of frequencies for the low and high turbulence inflow cases.

Figure 16 shows the power spectra of the turbulent flow velocity fluctuations in the turbine wake with the measurement point located at the downstream location of ($X/D = 0.5$, $Y/D = 0.0$, $Z/D = 0.5$), i.e., along the shedding path of the tip vortices in the PIV measurement plane. As visualized clearly in the “phase-locked” PIV measurement results given in Figs. 14 and 15, the measurement point would be at the upstream of the concentrated wake vortex breakdown for the low turbulence inflow case (i.e., the concentrated wake vortex breakdown at the downstream location of $X/D \approx 0.8$ for the low turbulence inflow case). However, the same measurement point would be located at the downstream of the concentrated wake vortex breakdown position for the high turbulence inflow case (i.e., the concentrated vortex breakdown at $X/D \approx 0.4$ for the high turbulence inflow case). Since very similar features were also seen in the power spectra of the horizontal (i.e., S_v spectra) and vertical (i.e., S_w spectra) components of the turbulent flow velocity vector, only the power spectra of the streamwise (i.e., S_u spectra) component of the turbulent flow velocity vector were presented in Fig. 16 for comparison.

As shown in the Fig. 16(a), for the case with relatively low turbulence intensity levels in the incoming flow, the classical turbulence energy production subrange and inertial subrange in the turbine wake flow, which are identified as the regions that follow power law scaling with -1 and $-5/3$ slopes, respectively, can be seen clearly in the power spectra of the streamwise (i.e., S_u spectra) component of the turbulent flow velocity. Similar features about the energy production and inertial subranges were also reported by Chamorro *et al.*⁹ and Zhang *et al.*²⁰ in quantifying the flow characteristics of turbine wakes. Furthermore, since the measurement point is located at the upstream position of the concentrated wake vortex breakdown for the low turbulence inflow case, localized high-energy signatures or the tip vortices can be identified easily in the spectra plots in terms of well-defined local peak frequencies. The well-defined local peak frequencies in the spectra plots are found to correspond well to the primary shedding frequency of the tip vortices from the rotating turbine blades (i.e., $3f_0$, where f_0 is the rotational frequency of wind turbine). Other high peaks, representing the harmonic frequencies of the shedding frequency of the tip vortices, can also be identified clearly from the spectra plots.

However, for the case with much higher turbulence intensity levels in the incoming ABL wind, while the turbulence energy production and inertial subranges in the wake flow (i.e., the regions with -1 and $-5/3$ slopes in the spectrum plots) can still be seen in the spectra plot given in

Fig. 16(b), no obvious high-energy containing signatures can be seen in the spectra plot. This is because the concentrated, high-energy containing wake vortices shedding from the rotating turbine blades have already broken down and turn into much smaller turbulent eddies before reaching to the measurement point. Therefore, the signatures of the concentrated, high-energy containing wake vortices cannot be identified easily in the power spectra of the measured turbulent velocity in the turbine wake for the high turbulence inflow case.

IV. CONCLUSION

A comparative study was conducted to investigate the turbine wake characteristics and dynamic wind loads acting on a model wind turbine placed in two different types of ABL winds with distinct mean and turbulence characteristics. A scaled three-blade HAWT model was used for the comparative study to simulate the scenario with the same wind turbine sited in the two different types of ABL winds. In addition to measuring the dynamic wind loads acting on the model turbine, a high-resolution PIV system was used to make both “free-run” and “phase-locked” measurements to quantify the flow characteristics and behavior (i.e., formation, shedding, and breakdown) of the unsteady wake vortices in the turbine wake. The detailed flow field measurements were correlated with the dynamic wind loading measurements in order to gain further insight into the underlying physics for the optimal design of the wind turbines operating in different ABL winds.

While the instantaneous wind loads acting on the model turbine were found to be highly unsteady with their magnitudes fluctuating significantly, the histograms of the dynamic wind loads acting the model turbine were found to be able to be fitted reasonably well by using Gaussian functions for the two studied cases with different turbulence levels in the incoming ABL winds. In comparison to those of the case with relatively low turbulence intensity levels in the incoming flow, the dynamic wind loads acting on the model turbine were found to fluctuate much more significantly for the high turbulence inflow case, which would result in much larger fatigue loads acting on the wind turbines, due to the much higher turbulence intensity levels in the incoming surface wind.

The PIV measurements reveal clearly that, since a portion of the kinetic energy carried in the incoming airflow was harvested by the wind turbine, the speed of the incoming surface wind would be decelerated after passing through the rotation disk of the turbine blades, which results in the velocity deficits in the turbine wake. The wake characteristics behind the wind turbine were found to be dominated by the behavior (i.e., formation, shedding, dissipation, and breakdown) of the unsteady wake vortices shedding from the rotating blades, nacelle, and tower of the wind turbine. In the near wake, the regions with high TKE and Reynolds stress levels were found to concentrate mainly along the shedding paths of the unsteady wake vortices. As moving downstream, the concentrated, high-energy containing wake vortices were found to be dissipated, and eventually break down into smaller turbulent eddies, which would cause a dramatic increase of the TKE and Reynolds stress levels in the turbine wake. The higher TKE and Reynolds stress levels in the turbine wake would result in enhanced turbulent mixing to promote the vertical transport of kinetic energy by entraining more high-speed airflow from above to re-charge the wake flow, thereby, to facilitate the recovery of the velocity deficits in the wake flow behind the model turbine.

In comparison with the low turbulence inflow case, the shedding of the concentrated wake vortices from the turbine rotor blades was found to become much more turbulent and random for the high turbulence inflow case due to the much higher turbulence intensity levels in the incoming surface wind. The breakdown of the concentrated wake vortices was also found to take place much earlier for the high turbulence inflow case, which contributes to the much higher TKE and Reynolds stress levels in the turbine wake, resulting in a much faster recovery of the velocity deficits in the turbine wake for the high turbulence inflow case, in comparison with that of the low turbulence inflow case.

ACKNOWLEDGMENTS

Supports from the National Science Foundation with Grant Nos. CBET-1133751 and CBET-1438099, and Iowa Energy Center with Grant No. 14-008-OG are gratefully acknowledged.

- ¹ Y. Sheinman and A. Rosen, "A dynamic model of the influence of turbulence on the power output of a wind turbine," *J. Wind Eng. Ind. Aerodyn.* **39**, 329–341 (1992).
- ² J. Lebron, L. Castillo, and C. Meneveau, "Experimental study of the kinetic energy budget in a wind turbine streamtube," *J. Turbul.* **13**, N43 (2012).
- ³ L. Chamorro and F. Porte-Agel, "A wind-tunnel investigation of wind-turbine wakes: boundary-layer turbulence effects," *Boundary-Layer Meteorol.* **132**, 129–149 (2009).
- ⁴ A. Ozbay, W. Tian, Z. Yang, and H. Hu, "An experimental investigation on the wake interference of multiple wind turbines in atmospheric boundary layer winds," in *AIAA-2012-2784, 30th AIAA Applied Aerodynamics Conference, New Orleans, Louisiana, 25-28 June 2012*.
- ⁵ L. J. Vermeer, J. N. Sorensen, and A. Crespo, "Wind turbine wake aerodynamics," *Prog. Aerosp. Sci.* **39**, 467–510 (2003).
- ⁶ J. Whale, C. G. Anderson, R. Bareiss, and S. Wagner, "An experimental and numerical study of the vortex structure in the wake of a wind turbine," *J. Wind Eng. Ind. Aerodyn.* **84**, 1–21 (2000).
- ⁷ I. Grant and P. A. Parkin, "DPIV study of the trailing vortex elements from the blades of a horizontal axis wind turbine in yaw," *Exp. Fluids* **28**, 368–376 (2000).
- ⁸ F. Massouh and I. Dobrev, "Exploration of the vortex wake behind of wind turbine rotor," *J. Phys.: Conf. Ser.* **75**, 012036 (2007).
- ⁹ L. Chamorro, R. Arndt, and F. Sotiropoulos, "Turbulent flow properties around a staggered wind farm," *Boundary-Layer Meteorol.* **141**, 349–367 (2011).
- ¹⁰ Z. Yang and P. Sarkar, "Visualization of the tip vortices in a wind turbine wake," *J. Visualization* **15**, 39–44 (2012).
- ¹¹ S. Schreck and M. Robinson, "Blade three-dimensional dynamic stall response to wind turbine operating condition," *J. Sol. Energy Eng.* **127**, 488–495 (2005).
- ¹² M. C. Robinson, M. M. Hand, D. A. Simms, and S. J. Schreck, "Horizontal axis wind turbine aerodynamics: Three-dimensional, unsteady, and separated flow influences," National Renewable Energy Laboratory, Technical Report No. NREL/CP-500-26337 (1999).
- ¹³ P. J. Moriarty, W. E. Holley, and S. P. Butterfield, "Extrapolation of extreme and fatigue loads using probabilistic methods," National Renewable Energy Laboratory, Technical Report No. NREL/TP-500-34421 (2004).
- ¹⁴ S. Lee, M. Churchfield, P. Moriarty, J. Jonkman, and J. Michalakes, "Atmospheric and wake turbulence impacts on wind turbine fatigue loading," National Renewable Energy Laboratory, Technical Report No. NREL/CP-5000-53567 (2011).
- ¹⁵ L. P. Chamorro and F. Porte-Agel, "Thermal stability and boundary-layer effects on wind turbine wakes: A wind tunnel study," *Boundary-Layer Meteorol.* **136**, 515–533 (2010).
- ¹⁶ L. P. Chamorro and F. Porte-Agel, "Turbulent flow inside and above a wind farm: A wind-tunnel study," *Energies* **4**, 1916–1936 (2011).
- ¹⁷ J. Lebron, L. Castillo, R. B. Cal, H. S. Kang, and C. Meneveau, "Interaction between a wind turbine array and a turbulent boundary layer," in *AIAA-2010-0824, 48th AIAA Aerospace Sciences Meeting including the New Horizons Forum and Aerospace Exposition, Orlando, Florida, 4-7 January 2010*.
- ¹⁸ R. B. Cal, J. Lebrón, L. Castillo, H. S. Kang, and C. Meneveau, "Experimental study of the horizontally averaged flow structure in a model wind-turbine array boundary layer," *J. Renewable Sustainable Energy* **2**, 013106 (2010).
- ¹⁹ H. Hu, Z. Yang, and P. Sarkar, "Dynamic wind loads and wake characteristics of a wind turbine model in an atmospheric boundary layer wind," *Exp. Fluids* **52**(5), 1277–1294 (2012).
- ²⁰ W. Zhang, C. D. Markfort, and F. Porte-Agel, "Near-wake flow structure downwind of a wind turbine in a turbulent boundary layer," *Exp. Fluids* **52**, 1219–1235 (2012).
- ²¹ H. Irwin, "The design of spires for wind simulation," *J. Wind Eng. Ind. Aerodyn.* **7**, 361–366 (1981).
- ²² B. L. Sill, "Turbulent boundary layer profiles over uniform rough surfaces," *J. Wind Eng. Ind. Aerodyn.* **31**, 147–163 (1988).
- ²³ Y. Q. Jia, B. L. Sill, and T. A. Reinhold, "Effects of surface roughness element spacing on boundary layer velocity profile parameters," *J. Wind Eng. Ind. Aerodyn.* **73**, 215–230 (1998).
- ²⁴ Y. Zhou and A. Kareem, "Definition of wind profiles in ASCE 7," *J. Struct. Eng.* **128**, 1082–1086 (2002).
- ²⁵ P. Jain, *Wind Energy Engineering* (McGraw Hill, 2007).
- ²⁶ American Society of Civil Engineering, ASCE 7-05 minimum design loads for building and other structures 2005.
- ²⁷ K. S. Hansen, R. J. Barthelmie, L. E. Jensen, and A. Sommer, "The impact of turbulence intensity and atmospheric stability on power deficits due to wind turbine wakes at Horns Rev wind farm," *Wind Energy* **15**, 183–196 (2012).
- ²⁸ *Architecture Institute of Japan, AIJ Recommendations for Loads on Buildings* (Architectural Institute of Japan, 1996).
- ²⁹ J. Locke and U. Valencia, "Design studies for twist-coupled wind turbine blades," Sandia National Laboratories, Technical Report No. SAND 2004-0522 (June 2004).
- ³⁰ R. E. Wilson, "Aerodynamic behavior of wind turbines," in *Wind Turbine Technology: Fundamental Concepts of Wind Turbine Engineering*, edited by D. A. Spera (ASME Press, 1994), pp. 215–282.
- ³¹ P. H. Alfredsson, J. A. Dahlberg, and P. E. J. Vermeulen, "A comparison between predicted and measured data from wind turbine wakes," *Wind Eng.* **6**, 149–155 (1982).
- ³² D. Medici and P. Alfredsson, "Measurement on a wind turbine wake: 3D effects and bluff body vortex shedding," *Wind Energy* **9**, 219–236 (2006).
- ³³ O. De Vries, "On the theory of the horizontal-axis wind turbine," *Annu. Rev. Fluid Mech.* **15**, 77–96 (1983).
- ³⁴ L. P. Chamorro, R. E. A. Arndt, and F. Sotiropoulos, "Reynolds number dependence of turbulence statistics in the wake of wind turbines," *Wind Energy* **15**, 733–742 (2011).
- ³⁵ T. Burton, D. Sharpe, N. Jenkins, and E. Bossanyi, *Wind Energy Handbook* (John Wiley & Sons Ltd, England, 2001).
- ³⁶ D. Medici, "Experimental studies of wind turbine wakes-power optimization and meandering," Ph.D. thesis (KTH Mechanics, Royal Institute of Technology, Sweden, 2005).